Fluid Mechanics of a Spinner-Flask Bioreactor

Philippe Sucosky, Diego F. Osorio, Jason B. Brown, G. Paul Neitzel

Georgia Institute of Technology, The George W. Woodruff School of Mechanical Engineering, 771 Ferst Drive, Atlanta, Georgia 30332-0405; telephone: 404-894-3242; fax: 404-894-8496; e-mail: paul.neitzel@me.gatech.edu

Received 26 February 2003; accepted 23 June 2003

Published online 27 October 2003 in Wiley InterScience (www.interscience.wiley.com). DOI: 10.1002/bit.10788

Abstract: Spinner-flask bioreactors have been used for the production of articular cartilage in vitro. The dynamic environment within bioreactors is known to significantly affect the growth and development of the tissue. The present research focuses on the experimental and numerical characterization of the flow field within a spinner flask operating under conditions used to produce cartilage. Laboratory experiments carried out in a scaled-up model bioreactor employ particle-image velocimetry (PIV) to determine velocity and shear-rate fields in the vicinity of the construct closest to the stir bar, in addition to turbulence properties. Numerical computations calculated using FLUENT, a commercial software package, simulate the flow field in the same model bioreactor under similar operating conditions. In the computations, scaffolds were modeled as both solid and porous media with different permeabilities and flow rates through various faces of the construct nearest the stir bar were examined. © 2004 Wiley Periodicals, Inc.

Keywords: tissue engineering; cartilage; spinner-flask bioreactor; particle-image velocimetry; computational fluid dynamics; porous media

INTRODUCTION

Bioreactors are cell-culture systems designed to enable the growth of engineered tissues. The biological and mechanical environments they provide must be controlled precisely to maximize process efficiency. The spinner-flask bioreactor is a simple cylindrical glass container in which growing tissues are suspended (Fig. 1a) and a stirring element located at the bottom of the tank ensures the mixing of the culture medium. When used to grow articular cartilage, biodegradable polymer scaffolds made of polyglycolic acid (PGA) are threaded onto needles to provide attachment sites for chondrocytes. Once attached, the chondrocytes express extracellular matrix (ECM), ultimately producing a solid piece of tissue. Among the components of ECM are glycosaminoglycan, a proteoglycan that gives articular cartilage its compressive strength, and type-II collagen, related to its tensile strength. Each needle usually holds three scaffolds separated by small silicone spacers as shown in Figure 1c. Two to four needles are inserted into the cap of the bioreactor, holding the tissue constructs in fixed positions within the reactor vessel.

Under certain culture conditions, three-dimensional cartilage of the desired shape and size can be grown. However, because of incompletely understood physiologic responses to external stimuli, the growth of tissue-engineered cartilage is far from routine. The mixing rate, mass-transfer rate, stress level and flow regime, all of which affect the biochemical composition and the morphology of the resulting tissue, are determined by the hydrodynamics of the bioreactor.

For cartilage, external mechanical forces have been shown to regulate the expression of extracellular matrix in vivo (Mow et al., 1991). Vunjak-Novakovic et al. (1996) found that bovine chondrocytes seeded under dynamic conditions and grown for 8 weeks in a turbulent spinner-flask were thicker, more homogeneous, stiffer, and contained more cells than constructs cultivated under static conditions. Freed and Vunjak-Novakovic (1995) studied the growth of articular cartilage within both the near-free-fall environment of the NASA rotating-wall bioreactor and a spinner-flask bioreactor. The different hydrodynamic environments existing in the two devices influenced the properties of the resulting tissues; cartilage grown in the rotating-wall vessel was characterized by fewer cells and more GAG than that grown in the spinner flask.

Freed et al. (1997) studied bovine chondrocytes cultured in rotating bioreactors fitted with a so-called ''viscous pump'' (Begley and Kleis, 2000, described below) and operated on both the Mir Space Station and on Earth. Constructs grown in Space were more spherical in shape and mechanically inferior than those grown on Earth in terms of aggregate modulus, hydrodynamic permeability, and dynamic stiffness. The principal difference between the two culture environments was the flow generated within the bioreactors. On Earth, the effect of gravity forced the constructs to settle and collide with the rotating-vessel wall

Correspondence to: Paul Neitzel

Contract grant sponsors: Office of Biological and Physical Research at NASA; the Georgia Tech/Emory Center for the Engineering of Living Tissues/National Science Foundation

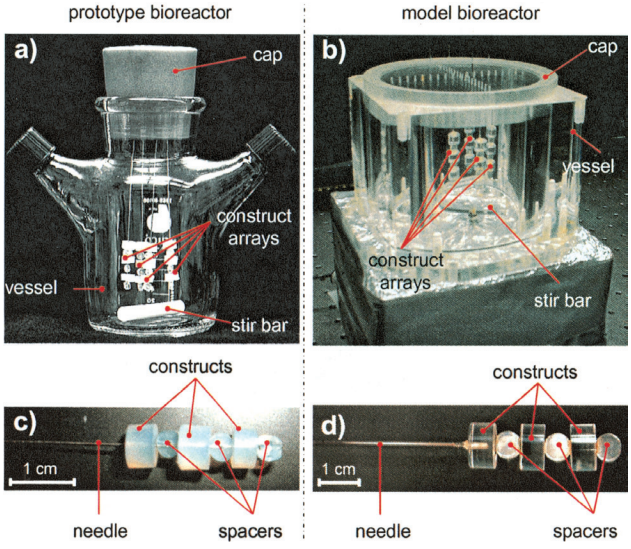

Figure 1. Prototype and model spinner-flask bioreactors. (a) Prototype bioreactor. The rotating stir bar at the bottom generates the mass transfer of the nutrients. (b) Model bioreactor made of acrylic and dynamically similar to the prototype flask. (c) Prototype construct array. The constructs are threaded onto four needles fixed in the cap of the vessel. (d) Model construct array made of acrylic.

while in Space, the constructs floated freely in the medium, following the flow driven by the viscous pump.

Gooch et al. (2001) have also addressed the effects of the hydrodynamic environment on tissue-engineered cartilage under both static and mixed conditions. Although increasing mixing rates stimulated the synthesis of GAG and collagen by the cells, they decreased the fraction of GAG retained by the constructs. Finally, more than the mixing intensity, the presence or absence of mixing was identified as the primary key parameter affecting the GAG and collagen content in the constructs.

Saini and Wick (2003) have subjected cartilage constructs to a controlled shear-stress environment through the use of a concentric-cylinder bioreactor. They found that cell counts, collagen, and GAG content per construct were all affected by the level of applied stress. The above observations support the hypothesis that dynamic flow conditions significantly affect the quality of cartilage grown within bioreactors. An additional consideration in subjecting tissues to the dynamic environment with a bioreactor is the fragility of mammalian cells. Because tissues grown in vitro are fixed on scaffolds (or, in other applications, on microcarrier beads), the relative motion between the tissue and the agitated fluid medium generated by the mixing exposes the cells to shear and normal stresses. One must ensure that these stresses are *locally* below levels that can cause harm to the growing tissue. Thus, it can be argued that to predict the behavior of tissues cultured within bioreactors one must understand both the local environment experienced by these tissues and the cause-and-effect relationship between the environment characteristics and the growing tissue. The present work is aimed at addressing the first of these needs for a particular bioreactor through the use of laboratory and numerical experimentation. Existing studies are few.

Experimental investigation of the flow field within a spinner-flask bioreactor as employed for tissue culture on microcarrier beads has been conducted using stereo particle-tracking velocimetry by Venkat et al. (1996). Their study focused on regimes characterized by high velocity gradients and are thus of particular relevance to microcarrier cultures. The assessment of cell damage was made by calculating the dissipation function (i.e., the rate of work done on a fluid element).

Begley and Kleis (2000) employed numerical methods to investigate the flow field within a rotating-wall, perfused vessel. The viscous pump is a solid disk mounted near one end of the reactor and rotated differentially with respect to the main body, acting as a centrifugal pump to circulate culture medium within the reactor, especially under conditions of microgravity. Their model, validated against laser-Doppler velocimetry measurements, was used to predict flow characteristics such as streamlines and mean shear-stress levels under both microgravity and terrestrial operating conditions.

Computational fluid dynamics methods have also been applied to the flow field within a roller-bottle bioreactor. Unger et al. (2000) have performed simulations using the commercial software package FLUENT for both creeping- and inertial-flow conditions.

As mentioned above, the aim of the present work is the characterization of the flow/shear-stress field within a spinner-flask bioreactor operating under conditions appropriate for the growth of cartilage. Parallel studies are in progress to ascertain the relationship between the local environment in the vicinity of a growing tissue and its resulting properties; these will be combined with the results of measurements and simulations to produce a tissue-growth model incorporating the characteristics of the dynamic environment [an existing tissue-growth model proposed by Obradovic et al. (2000) includes effects of diffusion alone]. Such a model would permit a rational determination of operating regimes necessary to achieve desired properties and possibly point the way to the design of new bioreactors for the development of tissue-engineered cartilage.

LABORATORY EXPERIMENTS: MATERIAL AND METHODS

Prototype Bioreactor

The prototype spinner-flask on which the model was based was provided by Drs. Freed and Vunjak-Novakovic of MIT and is shown in Figure 1a. The cylindrical glass flask contains four symmetrically positioned needles, each holding three cylindrical constructs made of PGA separated by cylindrical spacers made of silicone tubing (Fig. 1c). Mixing is done by a magnetic stirrer at the bottom of the vessel. When used for the growth of cartilage, the bio-

reactor is filled with 120 cm^3 of culture medium (density: ρ_p = 1.03 g/cm^3; kinematic viscosity: ν_p = 0.971 cSt—see Croughan et al., 1987) and stirred at 50 rpm (or an angular speed of ω_p = 5.24 rad/s). The dimensions and characteristics of the prototype flask are summarized in Table I. Consistent with the work of Vunjak-Novakovic et al. (1996), the length of the stir bar is chosen as the characteristic length and the velocity scale is based on the rotation speed N_p (in rev/s) and the length L_p of the stir bar, resulting in a Reynolds number for the bulk flow of

$$\mathrm{Re}_p = \frac{N_p L_p^2}{\nu_p} = 1758. \quad (1)$$

Model Bioreactor

The reliability of the PIV technique described below depends strongly on the quality of the optical-acquisition system, with refraction and deformation being major issues in a cylindrical system such as that employed for the present experiments. To avoid the refraction of the incident laser sheet and the light viewed orthogonally to it, a model bioreactor with plane external walls was designed. Refraction due to the curved inner wall of the vessel was compensated for by matching the refractive indices of the model bioreactor material and the model culture medium. The model spinner-flask was made of acrylic with a refractive index of n = 1.49. Hendricks and Aviram (1982) had found that an aqueous solution of zinc iodide is suitable for this refractive-index range. A solution with 60% zinc iodide, 38% distilled water, and 2% sodium bisulfite (percentages are by total mass) was used as the model culture medium (density: ρ_m = 1.90 g/cm^3, kinematic viscosity: ν_m = 1.68 cSt), to meet the refractive-index matching condition. To improve the optical access to the bioreactor, a 1.6:1-scale model vessel, constructs, and stir bar were designed as shown in Figure 1b and 1d. Dynamic similarity of the flows within the geometrically similar model bioreactor and prototype is achieved by matching the Reynolds number given in Eq. (1). From the knowledge of the prototype Reynolds number, the required model stir-bar rotation rate was 34 rpm. The measurements of the kinematic viscosity and the angular stir-bar velocity introduced an uncertainty of 8.9% on the desired value of the Reynolds number (Kline and McClintok, 1953; Wheeler and Ganji, 1995). Therefore, the Reynolds number at which the model bioreactor was operated can be estimated at 1758 $\pm$ 157. In the experiments, the four equiangularly spaced construct arrays were positioned at 25 mm from the center of the cap of the model bioreactor. The vertical distance between the lower surface of the bottom construct and the stir-bar was fixed at 10 mm. The stirring element was driven by a 0.9 degree, two-phase stepper motor (Oriental Motor PH266M-E06) through a gear train. The power was delivered by an electronic controller, enabling a smooth rotation and accurate control of the actual angular velocity. A tachometer attached to the base of the bioreactor and focused on the stir-bar axis was used to track the rotation speed and to index the angular position of the bar necessary for the phase-locked measurements that were required. Glass spheres (Potters Industries, 5000E) with a density of 2.54 g/cm^3 and a mean diameter of 11 μm were used as the flow-visualization tracers. When placed in the 1.89 g/cm^3 zinc iodide solution, the dynamic conditions within the bioreactor model prevented the particles from settling out of the flow, and for visualization purposes the low sedimentation rate (13.3 μm/s for 11 μm particles) was not expected to lead to significant error in the velocity measurements.

Table I. Characteristics and operating conditions of the prototype and model bioreactors.

	Prototype bioreactor	Model bioreactor
Bioreactor material	Glass	Acrylic
Construct material	Polyglycolic acid (PGA)	Acrylic
Spacer material	Silicone tubing	Acrylic
Working fluid	Cell culture medium	Zinc iodide
Fluid kinematic viscosity	0.971 cSt	1.68 cSt
Fluid density	1.03 g/cm^3	1.90 g/cm^3
Fluid volume	120 cm^3	529 cm^3
Bioreactor diameter	6.50 cm	10.5 cm
Free-surface height	3.8 cm	6.1 cm
Stir-bar length	4.52 cm	7.24 cm
Stir-bar diameter	0.787 cm	1.27 cm
Construct diameter	0.693 cm	1.12 cm
Construct thickness	0.377 cm	0.607 cm
Spacer diameter	0.396 cm	0.638 cm
Spacer thickness	0.168 cm	0.269 cm
Stirring rate	50 rpm	34 rpm

Particle-Image Velocimetry

Particle-image velocimetry (PIV) is an experimental technique employing optical and statistical methods to determine the instantaneous velocity field on a plane within a flow field. This technique has been studied extensively and improved during the last few years (Adrian, 1991; Willert and Gharib, 1991; Westerweel, 1997). The flow to be measured is seeded with small tracer particles and illuminated with a light sheet from a laser in the present experiments. By comparing the position of the illuminated particles at two instants of time and performing cross-correlation, it is possible to deduce the instantaneous displacement, and hence, velocity components at every location in the illuminated plane.

In the present experiments a double-head Nd:YAG laser (New Wave Reasearch Minilase III) was used to generate a pulsed output beam with a wavelength of 532 nm, an energy of 50 mJ and a pulse length of 5–7 ns. The beam was optically focused and formed into a light sheet with the use of mirrors and lenses. The thickness of the light sheet at the vessel axis was approximately 1 mm.

A Pulnix progressive-scan camera with a resolution of 768 × 484 pixels, a Navitar 50 mm TV lens and a 20 mm

extension were used to acquire images of the flow. An Imagenation frame grabber (PX610) was coupled to a Pentium Pro 200 computer (96 Mb of RAM, 3 Gb of storage capacity) to capture the pictures and convert them from NTSC to 8-bit bmp format. Because of limitations in computer storage capacity, the acquisition software was modified to record 320 × 240-pixel cropped frames, imaging a 0.91 cm × 0.69 cm area. An electronic circuit (with inputs from the tachometer and the NTSC video signals and outputs to the frame grabber and laser controller) was integrated with the PIV apparatus to enable phase-locked frame capturing. The PIV images were analyzed by a MATLAB program featuring a fast-Fourier transform algorithm to perform the cross-correlation and a Gaussian fit to determine the cross-correlation peak. Filtering and smoothing of the data points was performed using a median filter.

Experimental Protocol

Because the value of the Reynolds number $\mathrm{Re}_m = \mathrm{Re}_p = 1758$ is much larger than the critical impeller Reynolds number of 1000 determined by Nagata (1975), the flow was expected to be completely turbulent. Due to the capability and storage limitations of the frame grabber and camera, we were able to capture 24 valid image pairs corresponding to an angular range of 310° for each stir-bar revolution. Because the flow is turbulent and unsteady in the mean, the determination of mean and turbulence flow quantities requires the use of ensemble, rather than time, averaging (Bradshaw, 1971). Each ensemble represents the flow at a given stir-bar orientation; averaging the velocity at each point in the flow field over several ensembles permits the determination of the appropriate mean and fluctuating velocities at each point. The requirement of ensemble averaging further requires that measurements be phase-locked, i.e., timed to the precise location of the stir bar at each of the 24 angular orientations described above. Storage requirements limited data collection to 200 series (each corresponding to one 24-position stir-bar revolution) of data and thus, 200 ensembles at each point in the field at each angular position. The capture of the first image of each series was triggered by the stir bar passing through the same fixed position.

The cross-correlation algorithm was implemented using an interrogation window of 32 × 32 pixels employing no shift between image pairs. The calculation of the Kolmogorov scale corresponding to the smallest eddies in the flow (based on the work of Cherry and Papoutsakis, 1988) was used to determine a grid resolution suitable to retrieve the details of the turbulence. A grid of 22 × 16 points equally spaced by 13 pixels was found to be a suitable compromise to collect sufficiently resolved data while limiting the CPU calculation time. This particular configuration producing an overlap of 60% between two neighboring interrogation windows permitted the acquisition of independent data since the measurement of two adjacent velocity vectors was based on two fairly different sets of tracer particles (Willert and Gharib, 1991).

Because the stir bar rotates in a clockwise direction when viewed from above, one expects a mean flow of the same sense; for the front construct array defined in Figure 2, this corresponds to flow from right-to-left. Thus, the plane crossing the median section of the front construct array should contain the main velocity component. For this reason, the laser sheet was set to illuminate this section of the flow containing the unit vectors ($\mathbf{e_1}$, $\mathbf{e_2}$) of the Cartesian reference frame ($\mathbf{e_1}$, $\mathbf{e_2}$, $\mathbf{e_3}$) whose origin is located at the center of the bottom of the bioreactor (see Fig. 2). Because the rotation of the impeller plays a dominant role in the general flow pattern, PIV observations focused on the lower half of the bottom construct (i.e., that closest to the stir bar). In the reference frame ($\mathbf{e_1}$, $\mathbf{e_2}$, $\mathbf{e_3}$), the center of this construct has the coordinates $(x_1, x_2, x_3) = (0, 2.774, 2.500)$ cm. The bottom half of the construct was discretized into two subregions; the upstream and downstream regions are indicated in Figure 2. For each region, the 200 series of 24 phase-locked image pairs were recorded and processed with the PIV cross-correlation routine.

At each instant an image-pair was captured, the corresponding instantaneous velocity field $\mathbf{U}(\mathbf{x}, t)$ was computed. This field was obtained using the filtering and smoothing functions of the postprocessing code and yields the velocity field after spurious vectors (vectors that deviate significantly in magnitude and direction from nearby vectors) have been removed, both bad and spurious vectors have been replaced by a filtered average over neighboring vectors and a median filter has been applied. In order to quantify the magnitude of the velocity vectors, the resolution of the PIV images had to be determined.

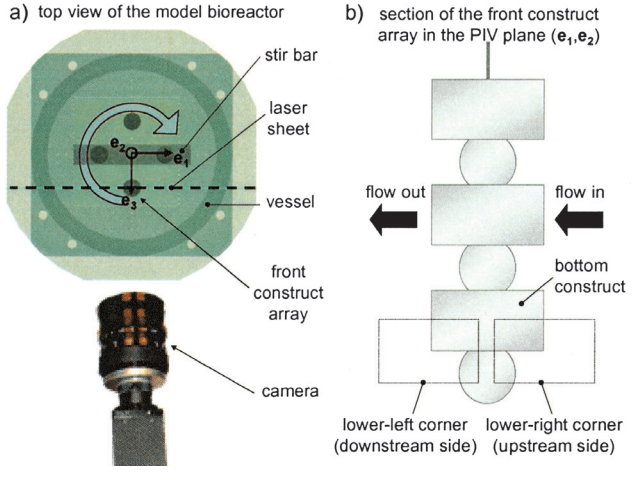

Figure 2. Experimental layout. (a) Top view of the model bioreactor. The laser sheet perpendicular to the camera passes through the center of the front construct array. The camera is placed perpendicular to the illuminated plane. The origin of the Cartesian coordinate system ($\mathbf{e_1}$, $\mathbf{e_2}$, $\mathbf{e_3}$) is located at the center of the bottom of the bioreactor. (b) Cross-section of the front construct array. The flow field was investigated in the lower right (i.e., upstream side) and lower left (i.e., downstream side) corners of the bottom construct.

The uncertainty on this measurement introduced a maximum uncertainty of 2.8×10^{-2} cm/s on the measurement of a vector magnitude of 4.0 cm/s (i.e., 0.7% uncertainty). Ensemble-averaging over the 200 series of data resulted in the determination of the mean-velocity field $\overline{\mathbf{U}}(\mathbf{x}, t)$ corresponding to time t in the rotation period. Subtraction of mean velocities from the corresponding instantaneous-flow velocities available at each instant of time yielded the fluctuating velocities $\mathbf{u}(\mathbf{x}, t)$ characterizing the turbulence, viz.,

$$\mathbf{u}(\mathbf{x}, t) = \mathbf{U}(\mathbf{x}, t) - \overline{\mathbf{U}}(\mathbf{x}, t) \tag{2}$$

Finally, the shear-stress field is computed to second-order accuracy from the velocity gradients using centered finite differences at interior grid points and forward or backward finite differences at boundary grid points.

The flow measurements were all conducted in the model bioreactor apparatus. The mean velocity and mean-shear stress can then be quantified in the prototype bioreactor using scaling considerations, i.e.,

$$\overline{\mathbf{U}}_p(\mathbf{x}, t) = \left(\frac{\nu_p L_m}{\nu_m L_p}\right)\overline{\mathbf{U}}_m(\mathbf{x}, t) \tag{3}$$

and

$$\overline{\tau_{ij}}_p(\mathbf{x}, t) = \left(\frac{\mu_p \nu_p L_m d_m}{\mu_m \nu_m L_p d_p}\right)\overline{\tau_{ij}}_m(\mathbf{x}, t). \tag{4}$$

Computational Methods

Conducted in conjunction with the laboratory experiments, the flow in the model bioreactor was simulated for the conditions considered in the experimental study. The computations were performed using the commercially available package FLUENT (Fluent Incorporated), which employs finite-volume methods. The geometry of the model reactor and its mesh were created using GAMBIT, a mesh-generator software package, as shown in Figure 3, where the different zones forming the geometry can be identified. The sliding zone at the bottom of the reactor was necessary for the simulation of the stir-bar motion using the sliding-mesh technique. Although the geometry employed for the simulations was constructed to be similar to that used in the experiments, a slight difference in construct positioning was observed a posteriori. Although the effect of discrepancies in the radial and vertical construct positions on the flow properties cannot be precisely estimated, it is expected to affect the agreement between experimental and numerical flow results, as discussed later.

The TGrid meshing option within GAMBIT was used to generate the mesh. TGrid creates a mesh that consists primarily of tetrahedral mesh elements but may also contain hexahedral, pyramidal, and wedge mesh elements where appropriate. Using the TGrid option and a spacing of 0.2 cm, an initial mesh containing 303,743 cells was

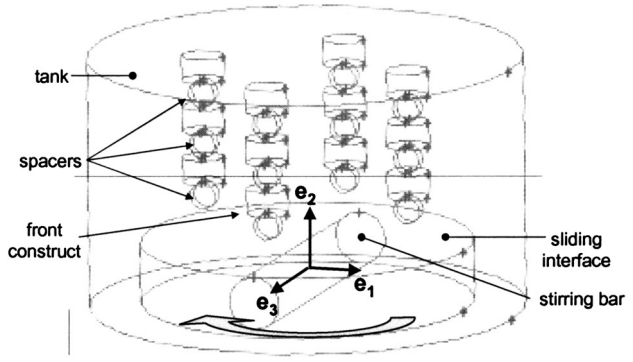

Figure 3. Geometry used for simulations showing the different zones. The Cartesian coordinate system ($\mathbf{e}_1$, $\mathbf{e}_2$, $\mathbf{e}_3$) centered on the lower face of the bioreactor is the same as that used for the PIV measurements (see Fig. 2).

obtained. The grid adaptation feature in FLUENT was then employed to further refine the mesh. Due to the high number of cells, we focused attention on the lowest construct on the needle (i.e., that nearest the stirring bar). A distance of six cells from the construct walls was chosen for refinement. After refinement, a total of 415,307 cells were obtained, and the smallest cell size was reduced by a factor of approximately 5.

FLUENT uses a control-volume approach to integrate the governing equations over each cell in the mesh, resulting in a set of discrete algebraic equations to be solved for the flow variables (i.e., velocity, pressure, etc.). The resulting equations are linearized and solved by different numerical techniques. In this fashion, all the fluid variables are found at each cell node after which the flux of each variable through the cell faces is obtained by interpolation. FLUENT offers two different methods for solving the governing equations known as the segregated and the coupled solvers. The segregated method performs iterations to solve the nonlinear governing equations sequentially, starting with the momentum equations, the continuity equation, and finally equations for scalars, until convergence is obtained. The coupled solver solves the governing equations (i.e., momentum, continuity, and energy equations) simultaneously, while the turbulence and other scalar equations are processed sequentially. In addition, different schemes are available for the linearization and discretization of the governing equations. For the present investigation, the k-ε model (where k, the turbulent kinetic energy, and ε, the dissipation, are defined as

$$k(\mathbf{x}, t) = \frac{1}{2}\overline{u_i(\mathbf{x}, t)u_i(\mathbf{x}, t)} \tag{5}$$

and

$$\varepsilon(\mathbf{x}, t) = 2\nu\overline{\frac{\partial u_i}{\partial x_j}(\mathbf{x}, t)\frac{\partial u_i}{\partial x_j}(\mathbf{x}, t)}, \tag{6}$$

respectively, (see Launder and Spalding, 1972) with standard constants and standard wall functions was

employed to model the turbulence and solve the Reynolds-averaged Navier-Stokes equations. For these calculations the segregated solver and implicit discretization were employed. In the implicit form, the unknown value for a given variable in each cell is computed using a relation that includes both existing and unknown values from neighboring cells, resulting in a system of linear equations with one equation for each cell in the domain.

The standard FLUENT interpolation scheme was used for the pressure that determines values at the element faces using the momentum-equation coefficients. For other quantities such as momentum and kinetic energy, the first-order-upwind interpolation scheme is used, in which the face value of any field variable is set equal to the cell-center value of the same variable in the cell immediately upstream of the point in question. All the simulations for the present investigation were performed in a computer equipped with one Pentium III-750 MHz processor, 256 MB RAM, and 19 GB of hard-disk space.

RESULTS

Experimental Results

Mean-Velocity Field

The observation of the mean-velocity field $\overline{\mathbf{U}}(\mathbf{x}, t) = \overline{\mathbf{U}}_1(\mathbf{x}, t)\mathbf{e}_1 + \overline{\mathbf{U}}_2(\mathbf{x}, t)\mathbf{e}_2$ computed by the PIV code in the upstream and downstream regions of the bottom half of the front construct invites some comments. An instantaneous mean-velocity field on the upstream side of the construct is shown in Figure 4b; at this location, the temporal variation over the course of an entire rotation period is rather small, except very close to the bar, as will be shown shortly. The flow is dominated by suction created in the low-pressure wake of the stir bar, drawing fluid down and to the left. Because of inertia, the fluid cannot follow the sharp angle between the vertical wall and horizontal lower surface of the construct and the flow separates, leading to the existence of a separation bubble between the lower surface of the construct and the cylindrical spacer, as observed in Figure 4b. In this region, the flow is nearly stagnant, compared with the main flow.

The mean-velocity field $\overline{\mathbf{U}}(\mathbf{x}, t)$ in the downstream region near the front construct is shown at an instant of time in Figure 4a. In the left portion of this region, the particles flow from top to bottom; this flow pattern persists over the entire period of the flow, indicating the strong suction created by the stir bar. A second region near the bottom of the window is characterized by large variations of the velocity field over the entire stir-bar revolution cycle. The mean velocity changes in both magnitude and direction, varying from strictly horizontal to strictly vertical flow. The drastic variations of the velocity in this region of the flow are obviously related to its proximity to the rotating bar. Finally, the flow separates at a point close to the lower surface of the construct for the same reasons as those described on the upstream side of the construct. Although the magnitudes of the velocity vectors in the upstream and downstream regions of the construct appear similar, different velocity scales have been used to construct Figure 4 and the velocity components on the downstream side of the flow are actually relatively small compared with those in the main flow region.

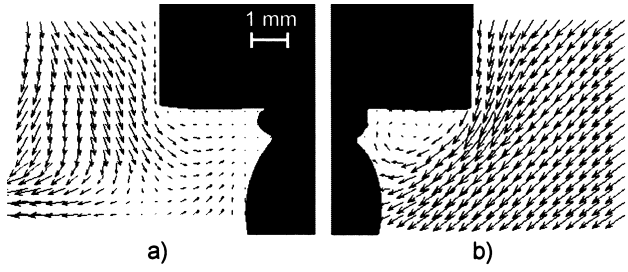

Figure 4. Snapshot of the mean-velocity field in the median plane of the model construct. On the upstream side (Fig. 4b), the fluid flows from the top-right corner to bottom-left corner of the picture. On the downstream side (Fig. 4a), the fluid flows from top to bottom and separates near the stir bar. Different velocity scales have been used to plot the velocity-vector fields in the upstream and downstream regions.

Flow Periodicity

The periodicity of the flow field in the upstream and downstream regions of the bottom construct was characterized by the time variation of $\overline{\mathbf{U}}(\mathbf{x}, t)$ at four pairs of points as shown in Figure 5. Vertical variations on the upstream and downstream sides of the construct are seen by examining points 1–2 (Fig. 5b) and points 5–6 (Fig. 5a), respectively. Corresponding horizontal variations are seen using points 3–4 (Fig. 5d) and 7–8 (Fig. 5c), respectively. The flow exhibits π-periodicity, as expected, with the magnitude of the variation decreasing with increased vertical distance from the stir bar (see, e.g., the vertical velocity at points 5–6). Periodicity is less evident at points immediately adjacent to construct surfaces (i.e., points 2–3–6–7) due to the retardation of both horizontal and vertical components of velocity in these regions.

Mean Shear-Stress Field

From the measurements of $\overline{\mathbf{U}}(\mathbf{x}, t)$, the instantaneous mean shear-stress field obtained in the PIV plane can be calculated from

$$\overline{\tau_{12}}(\mathbf{x}, t) = \mu\left(\frac{\partial \overline{U_1}}{\partial x_2}(\mathbf{x}, t) + \frac{\partial \overline{U_2}}{\partial x_1}(\mathbf{x}, t)\right), \qquad (7)$$

where $\overline{\mathrm{U}}_1(\mathbf{x}, t)$ and $\overline{\mathrm{U}}_2(\mathbf{x}, t)$ are the magnitudes of the horizontal and vertical components of the mean velocity, respectively, and μ is the dynamic viscosity of the liquid.

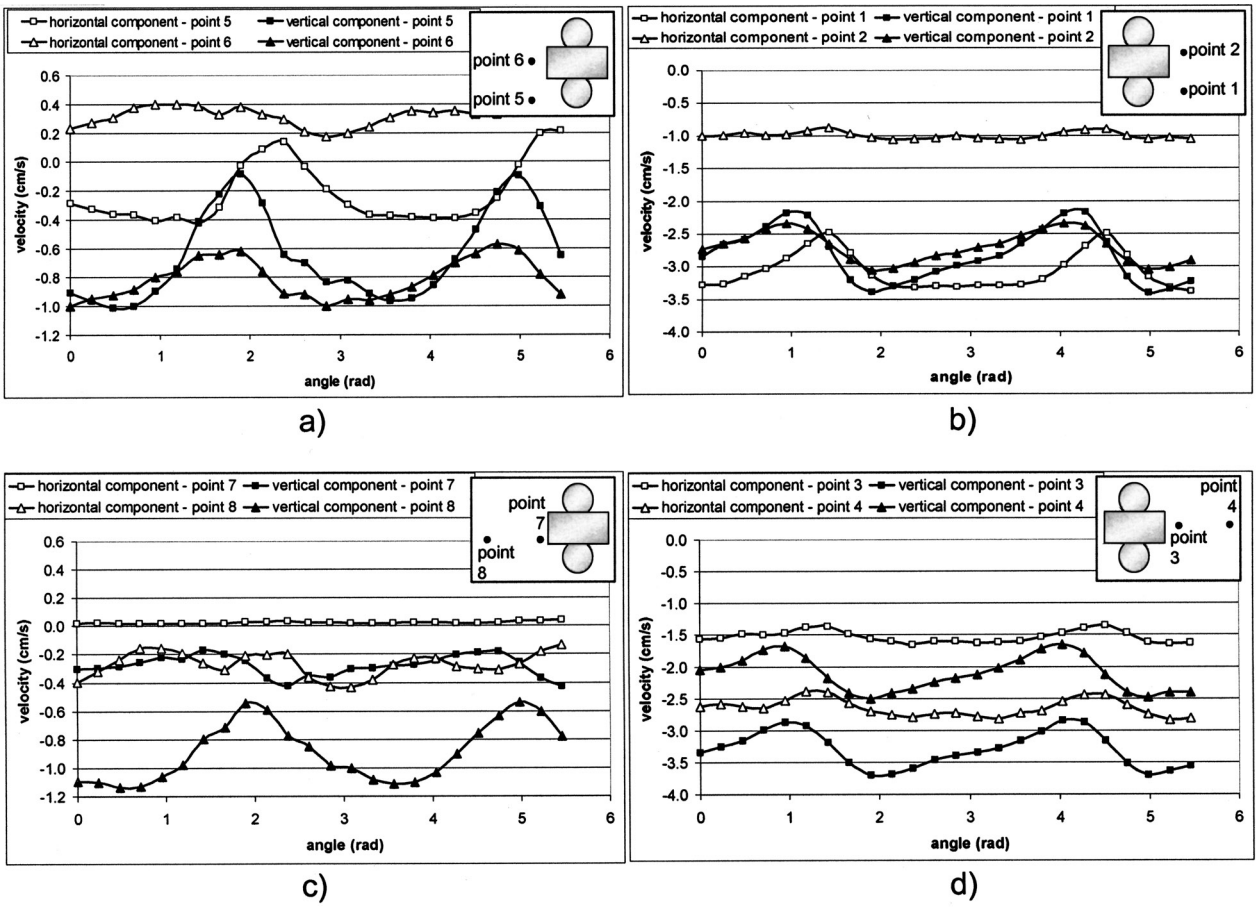

Figure 5. Time variation of $\overline{\mathbf{U}}(\mathbf{x}, t)$ at four pairs of points in the downstream (Fig. 5a,c) and upstream (Fig. 5b,d) regions of the bottom construct.

The mean shear-stress field captured at an instant of time in the vicinity of the upstream side of the construct surface is illustrated in Figure 6b. The shear stress is dominated by the $\mu \frac{\partial \overline{U}_2}{\partial x_1}$ contribution and the existence of a viscous boundary layer on the construct surface. The shear stress attains its maximum value at the sharp corner at the intersection of the vertical wall with the lower surface of the construct, where the flow separates from it, and continues to remain high in the shear layer associated with the observed separation bubble. Due to the proximity of this construct model to the stir bar, a large mean shear-stress (0.25 N/m^2 in the model, 0.11 N/m^2 in the prototype) is attained in this region of the flow. As expected, observations of the mean shear-stress field history show that this quantity is also π-periodic.

The analysis of the mean shear-stress field $\overline{\tau_{12}}$ at an instant of time in the downstream region of the flow is presented in Figure 6a. As in the upstream region, the wall effect produces a large gradient of the vertical component of the mean velocity along the vertical edge. This gradient corresponds to a region of high shear-stress. As before, the maximum mean shear-stress is experienced at a point close to the lower surface of the construct where the flow separates. This point is, in fact, characterized by high velocity gradients in both the horizontal and vertical directions. The maximum magnitude of 0.06 N/m^2 in the model (i.e., 0.03 N/m^2 in the prototype) is one fourth that measured on the upstream side. The shear layer associated with separation also generates a shear-stress. As a result, an elevated mean-shear stress distribution exists here as well. Finally, because the separation region is characterized by relatively small velocities, the corresponding shear-stress level is also low, especially along the lower surface of the scaffold.

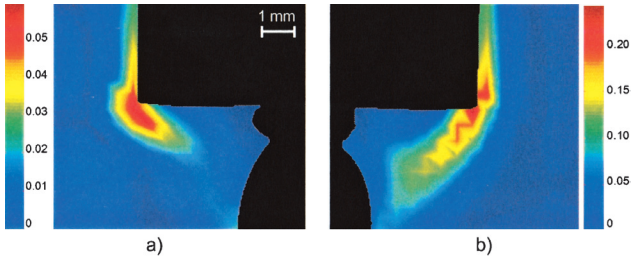

Figure 6. Snapshot of the mean-shear stress field in the median plane of the model construct (units are N/m^2). In both the downstream (Fig. 6a) and the upstream (Fig. 6b) regions of the flow, the mean-shear stress is concentrated along the vertical edge, near the lower surface of the construct and at the periphery of the recirculation regions.

Reynolds-Stress Field

The Reynolds stress is an apparent stress due to nonlinear interactions of the turbulent fluctuations that characterizes the impact of the turbulence on the mean flow (Tennekes and Lumley, 1972). The component of this tensor that is calculable from available PIV data is defined as:

$$\tau_{12}(\mathbf{x},t) = -\rho\overline{u_1(\mathbf{x},t)u_2(\mathbf{x},t)} \qquad (8)$$

where ρ is the density of the fluid and $u_1(\mathbf{x}, t)$ and $u_2(\mathbf{x}, t)$ are the horizontal and vertical components, respectively, of the fluctuating velocity. The extraction of the fluctuating components of the velocity at discrete angular positions of the stir bar permits the calculation of the Reynolds-stress field over an entire cycle of the flow. In Figure 7 the intensity field of the Reynolds stress obtained in the downstream (Fig. 7a) and upstream (Fig. 7b) regions of the construct can be seen, at four instants of time over half a revolution of the stir-bar (corresponding to one period of the flow field).

In the upstream region, it can be seen that the Reynolds stresses are largest in the shear layer that separates from the sharp edge of the construct, as might be expected. In the vicinity of the construct surfaces, the Reynolds stress is very small, due to the inhibition of turbulent fluctuations by the solid walls. Although we observe the largest turbulent stresses in the shear layer, the maximum Reynolds stress obtained over one period is approximately 0.12 N/m^2 in the model (0.050 N/m^2 in the prototype). This value is half that of the maximum mean shear-stress in this region of the flow. This observation suggests the dominance of the mean shear-stress over the Reynolds stress near (at least) the lower tissue construct, at each instant of time for the conditions at which these experiments were performed. This observation is in agreement with the typical structure of turbulent flows in the viscous sublayer in a thin region near a wall characterized by the dominance of the laminar shear-stress over the turbulent shear-stress. A comparison of the quantitative results obtained for the mean shear-stress and Reynolds stress extracted from the experiments and scaled to the prototype is given in Table II.

In the downstream flow region (Fig. 7a), the Reynolds stress is very small over the entire cycle of the impeller. Thus, the influence of turbulence on the mean flow near the construct is negligible in this region. The Reynolds stress does not begin to increase until the lower-left side of the interrogation window is reached. Although the Reynolds stress is necessarily zero at the construct surface, it does

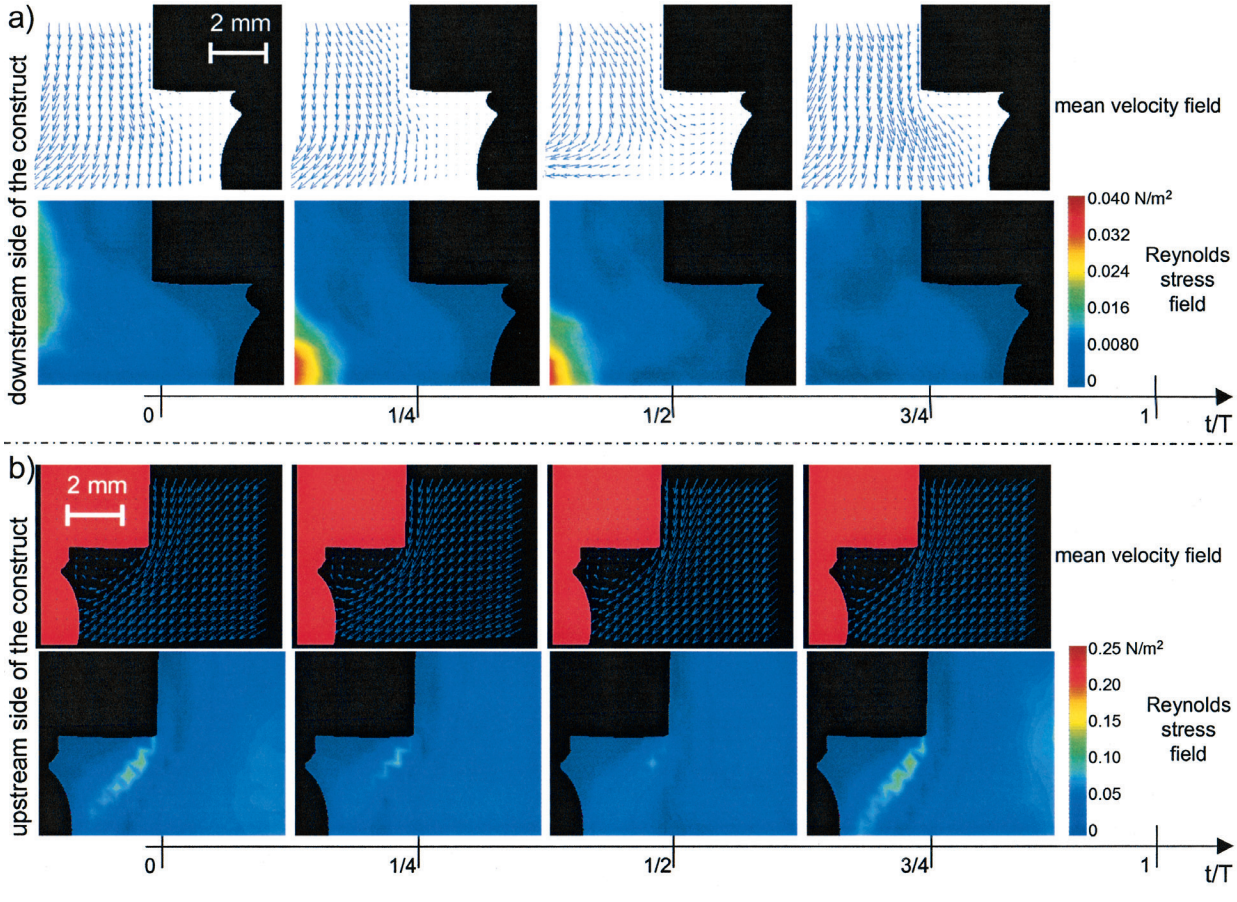

Figure 7. Evolution of the mean-velocity field and the Reynolds stress field in the downstream (Fig. 7a) and upstream (Fig. 7b) regions of the construct, over half a stir bar revolution (T). Units for the Reynolds stress are N/m^2.

Table II. Maximum values of the mean-shear stress and the Reynolds stress obtained experimentally in the upstream and downstream sides of the bottom half of the lower construct.

	$\overline{\tau}_{12\,\max}$ Model	$\overline{\tau}_{12\,\max}$ Prototype	$\tau_{12\,\max}$ Model	$\tau_{12\,\max}$ Prototype
Downstream side	0.06 N/m^2 (0.6 dyn/cm^2)	0.03 N/m^2 (0.3 dyn/cm^2)	0.04 N/m^2 (0.4 dyn/cm^2)	0.02 N/m^2 (0.2 dyn/cm^2)
Upstream side	0.25 N/m^2 (2.5 dyn/cm^2)	0.11 N/m^2 (1.1 dyn/cm^2)	0.12 N/m^2 (1.2 dyn/cm^2)	0.05 N/m^2 (0.5 dyn/cm^2)

play a role in the redistribution of momentum, impacting mean-flow velocity gradients. The maximum value of the Reynolds stress within this interrogation window is approximately 0.04 N/m^2 for the model (0.02 N/m^2 for the prototype) and is localized near the stir bar. Finally, the maximum Reynolds stress level has to be compared with the maximum value of 0.11 N/m^2 found in the upstream region. The net decrease of Reynolds stress from the upstream to the downstream side of the scaffold can be explained by the presence of the construct, constituting an obstacle in the path of the main flow.

Turbulence-Intensity Field

Finally, the level of turbulence in the model vessel was evaluated by calculating the turbulence-intensity field, which is determined in terms of the root-mean-square velocity fluctuation:

$$I(\mathbf{x},t) = \left(\overline{u_1{}^2(\mathbf{x},t) + u_2{}^2(\mathbf{x},t)}\right)^{\frac{1}{2}} \tag{9}$$

The distribution of the turbulence intensity field in the downstream and upstream flow regions in the PIV plane at an instant of time is depicted in Figure 8. As expected, the description of the turbulence intensity on the upstream side of the construct (Fig. 8b) is characterized by the same patterns already discussed in terms of the mean-velocity and Reynolds-stress distributions. In contrast with the properties of the upstream region, the shear layer generated by the lower-left corner is not characterized by high turbulence levels. In fact, the analysis of the Reynolds stress showed that the magnitude of the fluctuating components of the velocity were negligible in this region of the flow. Near solid surfaces, $I(\mathbf{x}, t)$ is small due to their suppression of turbulence.

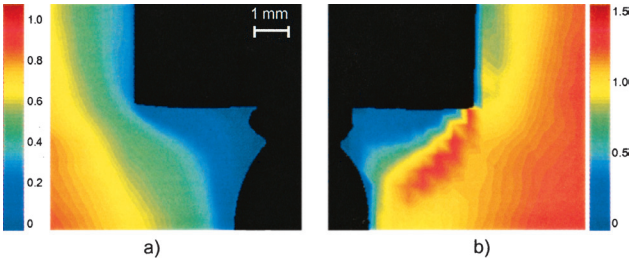

Figure 8. Snapshot of the turbulence intensity field in the median plane of the model construct (units are cm/s). In the downstream region (Fig. 8a), the intensity is mainly a function of the horizontal distance from the edge of the construct. In the upstream region (Fig. 8b), the intensity is almost zero near the wall and increases far from the construct.

Computational Results

Initially, all the constructs were defined as solid structures, in accordance with those used in the experiments and corresponding to tissue grown to confluence. The initial bar position aligned with the $\mathbf{e}_3$-axis, defining the origin $\theta = 0$ of a local azimuthal coordinate is shown in Figure 3. The initial condition was assumed to be a state of rest, bar rotation commenced at $t = 0$ and a time step was chosen corresponding to roughly 40 time steps per stir-bar revolution. Because it is the steady-state (*not* steady in the traditional sense of $\partial/\partial t = 0$) behavior that is of interest, it was necessary to determine the period of time following the initiation of stir-bar rotation necessary for start-up effects to disappear. To determine this, computations were performed for a representative case (33 rpm rotation rate) and the velocity history at a reference point located near the lower surface on the upstream side of the reference construct was examined. Because the stir bar is symmetric about its center, the Reynolds-averaged velocities should, at steady state, be time-periodic with a periodicity equal to half a revolution. As can be seen in Figure 9, the horizontal and vertical components of the velocity sampled at half-revolution times at the reference point $(x_1, x_2, x_3) = (0.686, 2.625, 2.630)$ located on the upstream side of the lower, front construct indicate that transient effects become negligible after approximately 40 seconds (i.e., roughly 22 stir-bar revolutions).

To assess the validity of these first results, the velocity history near the lower surface on the downstream side of the bottom construct $(x_1, x_2, x_3) = (-0.686, 2.625, 2.630)$

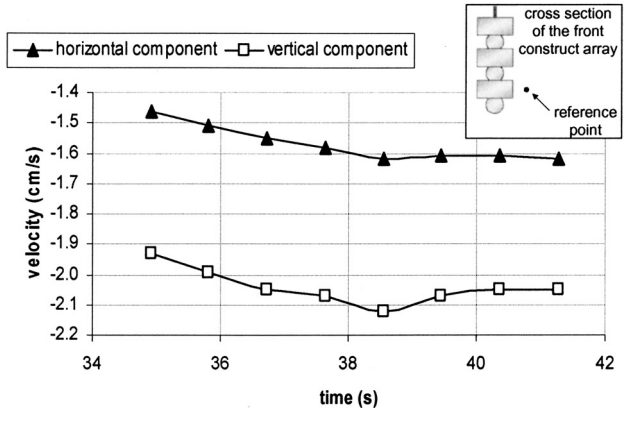

Figure 9. Histories of the horizontal and vertical components of the mean velocity sampled at half-revolution times at the reference point (0.686, 2.625, 2.630). Transient effects become negligible after 40 seconds (i.e., 20 stir-bar revolutions).

cm was compared with experimental results. The comparisons are presented in Figure 10; although the two velocity components are not in identical agreement with the experimental results, it can be appreciated that both the trends and amplitudes of the velocities are similar.

More detailed computations were performed for a stir-bar rotation rate of 34 rpm, corresponding to a Reynolds number of 1758. The time step in this case was chosen to be 0.02263 s, meaning that roughly 80 time steps (corresponding to a bar rotation of 4.5° per time step) were performed per revolution. The fact that the flow was π-periodic in θ was used, requiring that calculations for only one-half revolution following attainment of steady-state be performed. The CPU time per iteration was approximately 1 min, and, with the system requiring roughly 10–15 iterations for convergence, a computation time of 15 min per time step or 10 h per half-revolution is required. The data files occupy 70 MB of hard-disk space.

A comparison between calculated and experimental results for the horizontal component of the velocity at a reference point $(x_1, x_2, x_3) = (0.673, 2.625, 2.610)$ cm near the lower surface on the upstream side of the lowest front construct is presented in Figure 11. It may be observed that, although the value of the velocity is not the same (the predictions differing from the experiments by roughly 20%), the trends of the two histories are. Similar behavior was obtained for the vertical component of the velocity at this point and for other points in the same zone. The observed differences between experimental and numerical results can be attributed to the geometrical discrepancies between the model bioreactor used in the experiments and that used for the computations (discovered a posteriori, as noted earlier). In the simulations, the center of the bottom construct was localized at the coordinates $(x_1, x_2, x_3) = (0, 3.110, 2.610)$ cm as compared with (0, 2.774, 2.500) cm in the model used in the experiments.

Of principal interest in performing these simulations are estimates of the flow characteristics inside the spinner flask

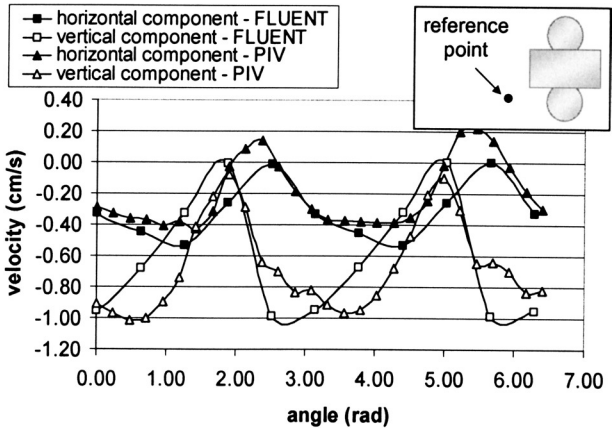

Figure 10. Comparison of velocity components obtained by FLUENT with results obtained by PIV experiments (ensemble-average achieved over 200 realizations). Angular speed 34 rpm, reference point (– 0.686, 2.625, 2.630).

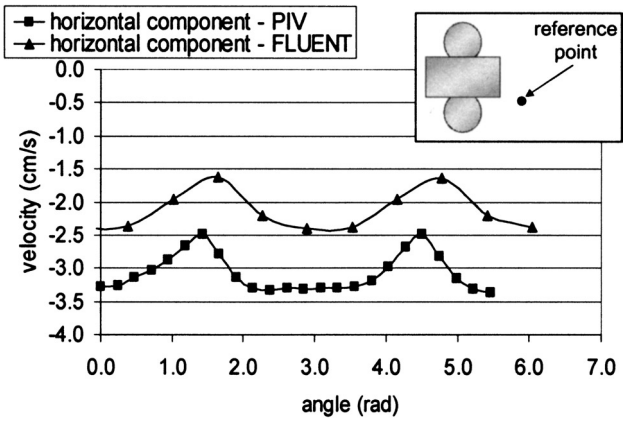

Figure 11. Comparison of the horizontal velocity obtained by FLUENT with results obtained by PIV experiments (ensemble-average achieved over 200 realizations). Angular speed 34 rpm, reference point (0.673, 2.625, 2.61).

of particular relevance to tissue growth. The velocity vectors for the plane $x_2 = 0$ with the bar at position $\theta = 0$, showing the mirror-image nature of the left- and right-hand sides of the flow with the stir bar in this position, as well as the varying flows experienced by constructs at different distances from the stir bar can be seen in Figure 12.

Once the velocity field is determined, the shear-stress distribution on the construct surfaces may be computed. The three shear-stress components and their magnitudes were calculated for each time step and the maximum values determined. Figure 13 depicts the wall-shear stress $\tau = \overline{\tau}_{12}^2 + \overline{\tau}_{23}^2 + \overline{\tau}_{13}^2$ evaluated on the construct surface and indicates the locations at which the maximum occurs for both the computations and the experiments. The maximum computed value of the shear stress is 0.283 N/m^2 (0.116 N/m^2 in the prototype). Based on this comparison, numerical results for the $\overline{\tau}_{12}$-component of the mean-shear stress were extracted for the same plane used for the PIV measurements. The distribution of this stress component on the

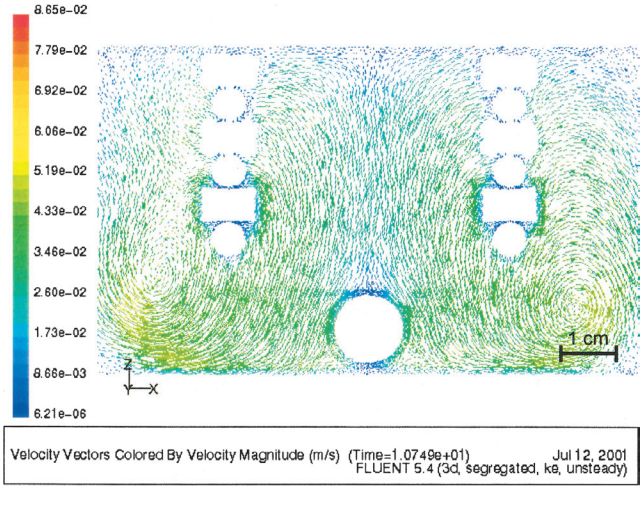

Figure 12. Velocity vectors for plane $x_2 = 0$. Angular speed 34 rpm and bar at $\theta = 0°$ (units are cm/s).

upstream side of the bottom construct at a representative instant of time is shown in Figure 14. In agreement with the experimental results, the numerical model localizes the maximum shear stress obtained in this section near the lower surface and along the vertical wall of the construct. Quantitatively, the maximum value of $\overline{\tau_{12}}$-calculated by FLUENT in this region of the model reactor is 0.21 N/m^2 (0.092 N/m^2 in the prototype). The comparison with the maximum stress level measured experimentally in the same plane, at the same location (i.e., 0.25 N/m^2 in the model, 0.11 N/m^2 in the prototype) shows a 16% discrepancy, likely explained by the difference in the vertical position of the construct in the geometry used in FLUENT and that of the model reactor employed in the experiments. In the experiments, the construct was closer to the bottom of the reactor than in the simulations, experiencing higher velocities due the stir bar and thus, a higher mean-shear stress. These results are summarized in Table III.

Once the main flow characteristics were determined and the forces acting on the assumed-solid construct surfaces were quantified, simulations were performed with the construct modeled as a porous medium. For this purpose, the previous solid-construct results were used as initial conditions. The main quantity of interest in this case is the volume-flow rate of culture medium through the porous construct. A standard Darcy-law model (Whitaker, 1986) was used to take into account the porosity and permeability of the construct. Under Darcy's law, as applied to an isotropically permeable substance,

$$-\frac{K}{\mu}\nabla p, \tag{10}$$

where **U** is the velocity, K is the permeability, μ is the fluid viscosity and p is the pressure.

A typical PGA scaffold has a porosity (void/solid fraction) of roughly 97% prior to seeding with chondrocytes. As cartilage is produced through the expression of extracellular matrix by the chondrocytes, the porosity of the tissue decreases. The permeability, with dimensions of area, is proportional to the porosity, but its determination requires a measurement or detailed calculation of flow speed as a function of imposed pressure gradient for a well-defined medium. Consequently, the permeability of neither a tissue scaffold nor cartilage is known precisely. Therefore, calculations were performed for two different permeabilities of $K = 1$, and 10^{-6}m^2 and the flow rates through the construct faces were obtained as a function of the bar angle for the purposes of illustrating trends. On the basis of Stokes-flow computations through a periodic fibrous porous medium performed by Serrat (M.S. thesis, Mechanical Engineering, Georgia Institute of Technology, 2001), it is estimated that the first of these permeabilities would correspond to a construct that is basically absent, while the second would be appropriate for a very porous scaffold.

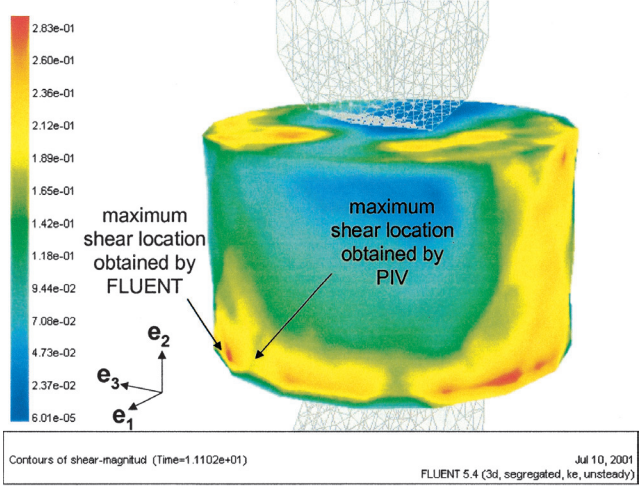

Figure 13. Maximum shear at construct surface showing the maximum shear location obtained by FLUENT simulations and PIV measurements. (PIV measurements obtained for the plane $x_2 = 2.625$).

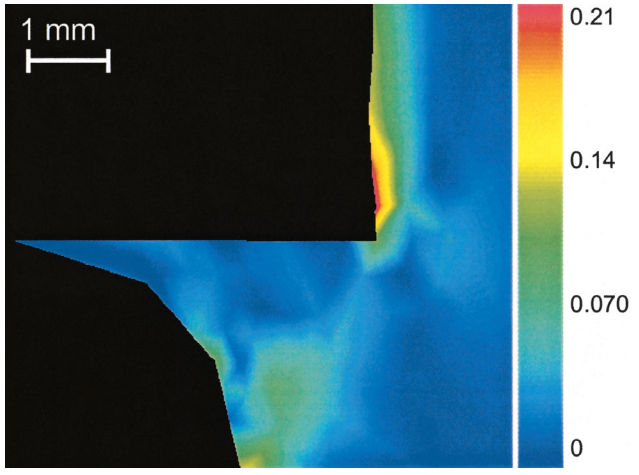

Figure 14. $\overline{\tau_{12}}$-component of the mean-shear stress obtained with FLUENT in the same plane as that used for the PIV measurements (i.e., plane $x_2 = 2.625$).

Table III. Maximum shear stress magnitude and pressure on reference construct surface and in PIV plane for bar rotating at 34 rpm. Results obtained for the model and the prototype.

		Model	Prototype
FLUENT	Maximum wall-shear stress over the construct	0.283 N/m^2	0.116 N/m^2
	Maximum shear stress ($\overline{\tau_{12}}$) in the PIV plane	0.210 N/m^2	0.0920 N/m^2
	Maximum pressure	3.02 Pa	1.37 Pa
PIV	Maximum wall-shear stress over the construct	N/A	N/A
	Maximum shear stress ($\overline{\tau_{12}}$) in the PIV plane	0.250 N/m^2	0.109 N/m^2
	Maximum pressure	N/A	N/A

A third-order-accurate Simpson's one-third rule was employed to numerically integrate the normal component of the velocity over the surfaces of the bottom, front construct to determine volume-flow rates. The flow rates through four control surfaces that comprise the entire construct surface (upstream face, downstream face, upper face, and lower face) as a function of the bar position for the two different permeabilities are shown in Figure 15. As expected, the maximum surface-flow rate occurs on the upstream-half (right) side of the construct, with the rest of culture medium entering the construct through the upper face (Fig. 15a). For higher permeability (Fig. 15b), however, a larger fraction of the flow is able to enter through its upper surface. Maximum medium flow rates of 1.9185 and 2.9877 cm^3/s were obtained for permeabilities of 10^{-6} and 1 m^2, respectively. These values correspond to 0.68110 and 1.0607 cm^3/s respectively, when scaled for the prototype bioreactor.

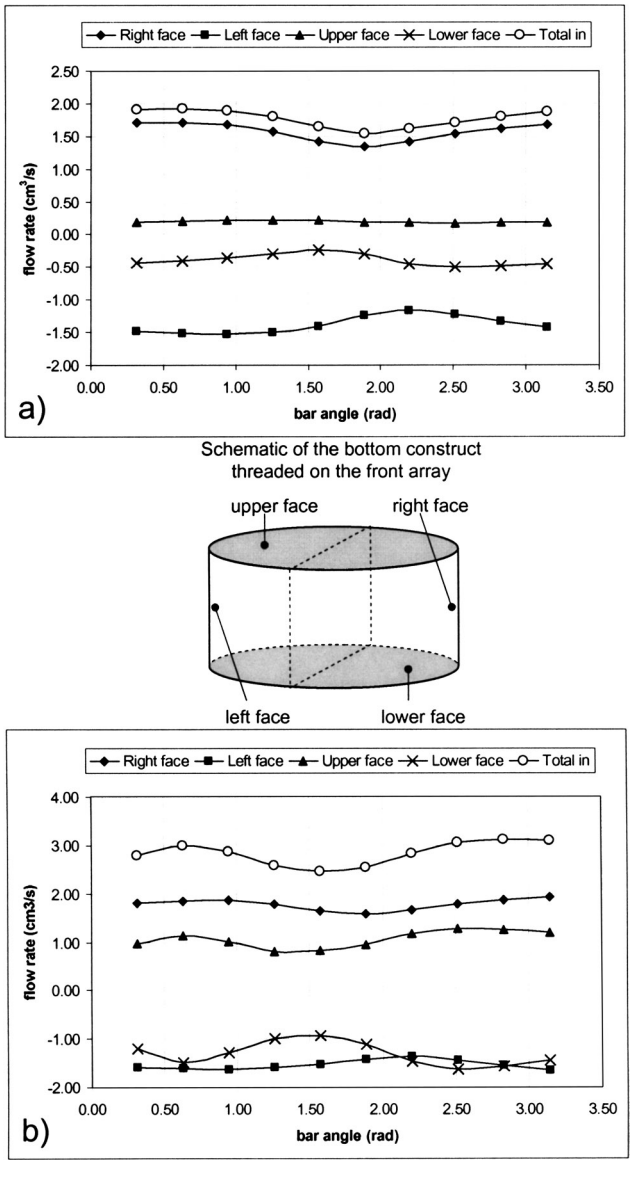

Figure 15. Culture medium flow rate per construct (cm^3/s) through the four construct faces when constructs were modeled as porous media with permeability $K = 10^{-6}$ m^2 (Fig. 15a) and $K = 1$ m^2 (Fig. 15b).

DISCUSSION

The flow field in the vicinity of a tissue construct within a spinner-flask bioreactor simulating normal operating conditions for the culture of cartilage has been characterized experimentally and numerically. The flow generated by the rotating stir bar is both turbulent and unsteady in the mean, posing challenges for both its measurement and numerical simulation. Experiments were performed in a model reactor constructed to remove index-of-refraction effects using phase-locked PIV and ensemble averaging to permit the extraction of turbulence quantities. Simulations were performed using the commercially available code FLUENT invoking a standard k-ε turbulence model. The results obtained from the experiments and computations are in reasonable agreement, particularly given the complex nature of the flow field.

The disadvantage of using a 2-D PIV system for the measurements relates to the 3-D nature of the flow field itself. However, the measurements reported herein were performed for that plane passing through a model tissue construct that lies in the principal (azimuthal) flow direction, ensuring that large velocities, and hence stresses, were likely to be encountered. Measurements have been conducted for the plane normal to that presented here, yielding velocities and stresses of lesser magnitude and so were omitted from this presentation of results. A comprehensive program of experiments characterizing all constructs within the reactor on a variety of planes is presently underway.

One might consider foregoing experiments on this flow field in light of the availability of packages such as FLUENT, given that the ultimate aim of this work is the development of a numerically based tissue-growth model for this flow. However, for a complex-turbulent flow of this nature it is unwise to accept the results of computations in the absence of independent experimental verification. The combined package of experimental and numerical results for this flow permits the use of each set for validation of the other. These first results are encouraging although further changes in the numerical model (e.g., the gridding or the choice of turbulence model) may be indicated by the more comprehensive results to follow. When ultimately validated for a range of conditions and used in conjunction with the tissue-growth model to be developed, the numerical simulations will permit the determination of operating states (and possibly alternate geometries) that will yield tissue of desired properties (e.g., specified GAG content). Thus, at this stage, it is important to use both laboratory and numerical experimentation and further work is necessary to identify the precise reasons for any disagreement between computation and experiment.

The numerical results also provide the first estimates of the flow rate through a porous felt as a function of time for two different construct permeabilities. The permeability of the scaffolds changes continuously with time during actual tissue growth due to cell attachment to the porous scaffold and the expression of extracellular matrix. It is envisioned that the computations to be performed following the development of the tissue-growth model will take the changing permeability of the construct into account.

The numerical determination of the flow characteristics within a spinner-flask bioreactor presents a significant challenge when all the phenomena involved in the system are taken into consideration. The presence of rotating turbulent flow, cylinders of small aspect ratio and differing orientations, porous media exposed to turbulent environments, and liquid-air interactions at the free surface all need to be taken into account for a complete picture of the flow experienced by a growing tissue construct to be obtained. The results presented here provide an enhanced understanding of in vitro culture of cartilage tissue in spinner-flask bioreactors. They constitute an initial step in the ultimate design of a reliable predictive tool (including a tissue-growth model incorporating the effects of culture-medium convection) for improving the operation of tissue-culture systems.

NOMENCLATURE

subscript m	characteristic of the model bioreactor	
subscript p	characteristic of the protoype bioreactor	
$\partial/\partial_{\mathbf{x}}$	partial derivative in the **e**1 direction	
$(\mathbf{e_1},\mathbf{e_2},\mathbf{e_3})$	Cartesian reference frame	
$\varepsilon(\mathbf{x},t)$	energy dissipation	(cm^2/s^2)
θ	angular position of the stir bar	(deg)
μ	dynamic viscosity of the fluid medium	$(g\ cm^{-1}\ s^{-1})$
ν	kinematic viscosity of the fluid medium	(cSt)
ρ	density of the fluid	(g/cm^3)
τ	wall-shear stress	(N/m^2)
$\overline{\tau_{ij}}\ (\mathbf{x}, t)$	component of the mean shear-stress tensor	(N/m^2)
$\tau_{ij}\ (\mathbf{x}, t)$	component of the Reynolds-stress tensor	(N/m^2)
$\boldsymbol{\omega}$	angular velocity of the stir bar	(s^{-1})
$I(\mathbf{x}, t)$	turbulence intensity	(cm/s)
$k(\mathbf{x}, t)$	turbulent kinetic energy	(cm^2/s^2)
K	permeability	(m^2)
L	stir-bar length	(cm)
n	index of refraction	(dimensionless)
N	stir-bar rotation speed	(rev/s)
p	pressure	(N/m^2)
Re	impeller Reynolds number	(dimensionless)
T	period of the stir bar	(s)
t	time	(s)
$\mathbf{u}(\mathbf{x},t)$	fluctuating-velocity vector	(cm/s)
$\mathbf{u}_i(\mathbf{x}, t)$	component of the fluctuating-velocity vector in the $\mathbf{e}_i$ direction	(cm/s)
$\overline{\mathbf{U}}\ (\mathbf{x}, t)$	mean-velocity vector	(cm/s)
$\overline{U_i}(\mathbf{x}, t)$	component of the mean-velocity vector in the $\mathbf{e}_i$ direction	(cm/s)
$\mathbf{U}(\mathbf{x}, t)$	instantaneous-velocity vector	(cm/s)
$U_i(\mathbf{x}, t)$	component of the instantaneous-velocity vector in the $\mathbf{e}_i$ direction (cm/s)	
$\mathbf{x}$	position vector with coordinates (x_1,x_2,x_3) in the $(\mathbf{e_1},\mathbf{e_2},\mathbf{e_3})$ coordinate system	

The authors wish to thank Drs. L. Freed and G. Vunjak-Novakovic of MIT for helpful discussions and for providing the prototype bioreactor on which the model used for these experiments was based.

References

Adrian RJ. 1991. Particle-imaging techniques for experimental fluid mechanics. Ann Rev Fluid Mech 23:261–304.

Begley CM, Kleis SJ. 2000. The fluid dynamic and shear environment in the NASA/JSC rotating-wall perfused-vessel bioreactor. Biotech Bioeng 70:32–40.

Bradshaw P. 1971. An introduction to turbulence and its measurement. Oxford: Pergamon Press. p 9.

Cherry RS, Papoutsakis ET. 1988. Physical mechanisms of cell damage in microcarrier cell bioreactors. Biotechnol Bioeng 32:1001–1014.

Croughan MS, Hamel JF, Wang DIC. 1987. Hydrodynamic effects on animal cells grown in microcarrier cultures. Biotechnol Bioeng 29: 130–141.

Freed LE, Langer R, Martin I, Pellis NR, Vunjak-Novakovic G. 1997. Tissue engineering of cartilage in space. Proc Nat Acad Sci 94:13885–13890.

Freed LE, Vunjak-Novakovic G. 1995. Cultivation of cell-polymer tissue constructs in simulated microgravity. Biotechnol Bioeng 46: 306–313.

Gooch KJ, Kwon JH, Blunk T, Langer R, Freed LE, Vunjak-Novakovic G. 2001. Effects of mixing intensity on tissue-engineered cartilage. BiotechNOL Bioeng 72:402–407.

Hendricks R, Aviram A. 1982. Use of zinc iodide solutions in flow research. Rev Scien Instr 53:75–78.

Kline SJ, McClintok FA. 1953. Describing uncertainties in single-sample experiments. Mech Eng 75:3–8.

Launder BE, Spalding DB. 1972. Lectures in mathematical models of turbulence. London: Academic Press.

Mow VC, Ratcliffe A, Rosnwasser MP, Buckwalter JA. 1991. Experimental studies on repair of large osteochondral defects at a high weight bearing area of the knee joint: A tissue engineering study. J Biomech Eng—Trans ASME 113:198–207.

Nagata S. 1975. Mixing—Principles and applications. NewYork: Wiley. p 458.

Obradovic B, Meldon JH, Freed LE, Vunjak-Novakovic G. 2000. Glycosaminoglycan deposition in engineered cartilage: Experiments and mathematical model. AIChE Journal 46:1860–1871.

Saini S, Wick TM. 2003. Concentric cylinder bioreactor for production of tissue engineered cartilage: Effect of seeding density and hydrodynamic loading on construct development. Biotech Prog 19: 510–521.

Tennekes H, Lumley JL. 1972. A first course in turbulence. Cambridge, MA: MIT Press. p 32–33.

Unger DR, Muzzio FJ, Aunins JG, Singhvi R. 2000. Computational and experimental investigation of flow and fluid mixing in the roller bottle bioreactor. Biotechnol Bioeng 70:117–130.

Venkat RV, Stock RL, Chalmers JJ. 1996. Study of hydrodynamics in microcarrier culture spinner vessels—A particle tracking velocimetry approach. Biotechnol Bioeng 49:456–466.

Vunjak-Novakovic G, Freed LE, Biron RJ, Langer R. 1996. Effects of mixing on the composition and morphology of tissue engineered cartilage. AIChE J 42:850–860.

Westerweel J. 1997. Fundamentals of digital particle image velocimetry. Measure Sci Technol 8:1379–1392.

Wheeler AJ, Ganji AR. 1995. Introduction to engineering experimentation. Englewood Cliffs, NJ: Prentice Hall. p 159–162.

Whitaker S. 1986. Flow in porous media I: A theoretical derivation of Darcy's law. Transp Porous Media 1:3–25.

Willert CE, Gharib M. 1991. Digital particle image velocimetry. Expts Fluids 10:181–193.